The Stability of Frictional Sliding on Dip-Slip and Finite Length Faults

Rob M. Skarbek*[1]

[1]Planetary Science Institute

1 Abstract

This paper examines the linear stability of sliding on faults embedded in a 2D elastic medium that obey rate and state friction and have a finite length and/or are near a traction-free surface. Previous work typically has examined either spring-slider systems or infinitely long faults. Results are obtained using a numerical technique that allows for analysis of systems with geometrical complexity, and/or heterogeneous material properties; however only systems with homogeneous frictional and material properties are examined. Some analytical results are also obtained for the special case of a fault that is parallel to a traction-free surface. On velocity-weakening faults with finite length, there is a critical fault length L^* for unstable sliding that is analogous to the critical nucleation length h^* that is usually derived from spring-slider or infinite fault systems. Faults longer than L^* are unstable to perturbations of any size. On vertical strike-slip faults or faults in a full-space $L^* \approx h^*/e$, where e is Euler's number. For dip-slip faults near a traction-free surface $L^* \leq h^*/e$ and is a function of dip angle β, burial depth d, and friction coefficient. In particular, L^* is at least an order of magnitude smaller than h^* on shallowly dipping ($\beta < 10°$) faults that intersect the traction-free surface. Additionally, $L^* \approx h^*/e$ on dip-slip faults with burial depths $d \geq h^*$. For sliding systems that can be treated as a thin layer, such as landslides, glaciers, or ice streams, $L^* = h^*/2$. Finally, conditions are established for unstable sliding on infinitely-long, velocity-strengthening faults that are parallel to a traction-free surface.

Key words: Friction, Instability analysis, Earthquake dynamics.

*rskarbek@psi.edu

2 Introduction

How does the geometry of fault systems affect the stability of frictional sliding? Most knowledge of frictional stability comes from analyses of spring-slider systems or systems consisting of an infinitely long fault in an infinite elastic medium (e.g. *Ruina*, 1983; *Rice and Ruina*, 1983; *Rice et al.*, 2001; *Uenishi and Rice*, 2003). These two systems do not include important aspects of fault geometry such as proximity to a traction-free surface, fault dip angle, or finite fault length. This paper examines the linear stability of sliding on finite length faults that obey rate and state friction (RSF) and are embedded in a 2D elastic continuum with homogeneous material properties. As in many previous studies, the focus here is on the quasi-static regime where inertia is neglected (e.g. *Rice and Ruina*, 1983; *Uenishi and Rice*, 2003; *Viesca*, 2016a,b; *Aldam et al.*, 2017; *Heimisson et al.*, 2019; *Ozawa et al.*, 2024).

The specific finite length geometries considered are: faults in an infinite full-space; faults parallel to a traction-free surface; and dip-slip faults and vertical strike-slip faults in a half-space. Including these features provides more accurate assessments of the sliding stability of natural fault systems. First, because all faults have a finite length and second, because many faults are near the surface of the earth or the seafloor. Additionally, landslides (*Handwerger et al.*, 2016), ice streams (*Lipovsky and Dunham*, 2017), and glaciers (*Zoet et al.*, 2020) also exhibit sliding behavior that can be described by frictional processes. The results show that these basic geometrical effects cause significant departures from long-standing results on stability behavior.

For a fault in an elastic medium, the stability of sliding can be assessed by considering a balance between the rate at which elastic stress stored in the fault system can be unloaded, and the rate at which shear stress on the fault is reduced (i.e. fault weakening) in response to sliding (e.g. *Scholz*, 2019). Unstable sliding initiates when the fault weakening rate is higher than the elastic unloading rate. In addition to earthquakes, slow frictional slip events (such as that occur in subduction zones and for example on the Whillians Ice Plain) are also a manifestation of unstable behavior since they involve episodic slip that is faster than the long term slip rate (e.g. *Bindschadler et al.*, 2003; *Schwartz and Rokosky*, 2007; *Bürgmann*, 2018).

For frictional sliding, the changes in shear stress on a fault are described by the RSF equations wherein the evolution of the friction coefficient μ on a surface is a function of the sliding rate v and an internal state variable θ

$$\mu(v, \theta) = \mu_0 + a \ln\left(\frac{v}{v_0}\right) + b \ln\left(\frac{v_0 \theta}{d_c}\right), \tag{1}$$

where μ_0 is a reference friction coefficient for steady state sliding at the reference velocity v_0, a and b are constitutive parameters, and d_c is a critical slip distance that is related to the amount of slip needed to attain a new steady state after changes in sliding velocity (*Dieterich*, 1979; *Ruina*, 1983; *Marone*, 1998). The reference values μ_0 and v_0 are not arbitrary, but are determined from experimental measurements of how the steady state friction coefficient of a given material depends on the sliding velocity. However, pairs of values (μ_0, v_0) can be chosen from amongst a set of such measurements. The evolution of the state variable is commonly described using the aging or slip laws:

$$\text{aging law:} \quad \frac{\partial \theta}{\partial t} = 1 - \frac{v\theta}{d_c}, \quad \text{slip law:} \quad \frac{\partial \theta}{\partial t} = -\frac{v\theta}{d_c} \ln\left(\frac{v\theta}{d_c}\right). \tag{2}$$

For velocity-weakening friction ($a - b < 0$; or $a/b < 1$), fault weakening will occur due to a reduction in the friction coefficient as sliding rate increases. Weakening can also occur due to a coupling between fault slip and changes in normal stress, which can lead to unstable behavior for velocity-strengthening friction below some critical value of a/b. This effect has been shown to exist on bimaterial and poroelastic faults (*Rice et al.*, 2001; *Ranjith*, 2014; *Heimisson et al.*, 2019), on faults with fault-valve behavior (*Ozawa et al.*, 2024), and on faults that lack geometric reflection symmetry across the sliding surface (*Aldam et al.*, 2016). Lack of geometric reflection symmetry is a very general feature of fault systems. So too then is the possibility of unstable behavior on velocity-strengthening faults. The results in this paper take a first step in establishing the range of parameters where this behavior occurs on faults that are near a traction-free surface.

Linear stability analysis of faults in an elastic continuum leads to the concept of a nucleation length h^* (*Ruina*, 1983; *Rice and Ruina*, 1983). The nucleation length is usually interpreted as the minimum length of a failing fault patch that is required for an unstable sliding event to develop (e.g. *Dieterich*, 1992; *Scholz*, 2019). In this interpretation, failure on velocity-weakening fault patches with lengths smaller than h^* cannot develop into an unstable event. The value of h^* is usually derived using one of two different methods.

First, h^* can be found analytically for the special case of an infinitely long fault with constant frictional properties and effective normal stress σ, embedded in an infinite, 2D elastic full-space with homogeneous properties. Allowing the fault to be infinitely long simplifies the mathematical analysis sufficiently to obtain an equation for h^*:

$$h_F^* = \frac{\pi G' d_c}{\sigma(b-a)} , \tag{3}$$

where G' is the effective shear modulus (*Rice and Ruina*, 1983; *Rice et al.*, 2001). Here the symbol h_F^* is used to denote the special value of the nucleation length for a homogeneous fault in a full-space. Because the derivation of h_F^* involves an infinitely long fault, its proper definition is the critical wavelength of an infinitely long perturbation to the slip velocity; perturbations with wavelengths smaller than h_F^* will not develop into unstable events (*Rice and Ruina*, 1983; *Rice et al.*, 2001). Therefore, in this analysis h_F^* does not represent a minimum contact or patch length.

Equation (3) without the factor of π can also be obtained by equating the critical stiffness of an RSF spring-slider system to the stiffness of a crack subjected to anti-plane strain conditions and a constant stress drop; other numerical prefactors are obtained depending on the assumed stress and strain conditions (see Table 1 in *Dieterich*, 1992). Assuming a single value of stiffness for a fault simplifies the mathematics and allows an equation for h_F^* to be obtained from a spring-slider analysis. However, the stiffness of a fault in an elastic continuum is a quantity that evolves through space and time as the fault slips (e.g. *Rice and Ruina*, 1983; *Horowitz and Ruina*, 1989).

When faults are not infinitely long or when a spring-slider model cannot capture important features of a fault system, then it becomes difficult to apply analytical methods of linear stability analysis. In this paper these difficulties are overcome by using a numerical method for conducting linear stability analysis of 2D finite length fault systems. The method can be applied to any fault system for which stress change functions are available (defined in the next section), and can accommodate features such as heterogeneous material properties or multiple faults. Analytical results are also obtained for the special case of a fault that is parallel to a traction-free surface.

The results of this paper show that a perturbation of any size will nucleate an unstable sliding event on a finite length fault once the fault length is larger than some critical value L^*. Throughout this paper, values of h^* are referred to as "critical wavelengths" and the symbol L^* is used to denote a "critical fault length". Subscripts are used for both h^* and L^* to differentiate between specific geometries. On vertical strike-slip faults or faults in a full-space, $L_F^* \approx h_F^*/e$ where e is Euler's number. For dip-slip faults near a traction-free surface, $L_D^* \leq h_F^*/e$ and is a function of dip angle, burial depth of the fault's up-dip edge, and friction coefficient. However, $L_D^* \approx h_F^*/e$ for dip-slip faults where the up-dip edge of the fault is buried at a depth greater than or equal to h_F^*. The results also establish conditions for linear instability under velocity-strengthening friction on infinitely long faults that are parallel to a traction-free surface. Finally, since the focus of this paper is on linear stability, behavior in the nonlinear regime (e.g. rupture localization or propagation) is not considered or examined.

3 Methods

3.1 Linear Stability Analysis

Consider a fault of length L that obeys equation (1) and either of equations (2), and denote the position along the fault by ξ. Assume also that the fault is embedded in a 2D homogeneous elastic medium with shear modulus G and Poisson ratio ν and define an effective shear modulus G' such that $G' = G$ for anti-plane sliding, and $G' = G/(1-\nu)$ for in-plane sliding. A linear stability analysis of the fault's sliding motion can be conducted according to the following steps. **(1)** Write the system of nonlinear equations governing the evolution of sliding velocity $v(\xi, t)$ and state variable $\theta(\xi, t)$ along the fault. **(2)** Determine a uniform steady state of the system such that $v(\xi, t) = v_0$ and $\theta(\xi, t) = \theta_0$. **(3)** Obtain a linearized system of equations by computing the Jacobian matrix $\boldsymbol{J}$ of the nonlinear system and evaluating it at the uniform steady state so that $\boldsymbol{J}_0 = \boldsymbol{J}(v_0, \theta_0)$. **(4)** Determine the stability of the linear system by examining the eigenvalues of $\boldsymbol{J}_0$. If any eigenvalue has a positive real part then the system is unstable.

Step 1. For quasi-static sliding, the velocity of the fault is governed by a balance between frictional resistance $\tau_F = \mu\sigma$ and the shear stresses resolved upon the fault $\tau = \tau_0 + \tau_E$, where τ_E is the change in shear stress due to gradients in slip along the fault, and τ_0 is the shear stress on the fault in the absence of any slip. As with the shear stress, the normal stress on the fault is $\sigma = \sigma_0 + \sigma_E$. The stress balance changes in time as $\dot{\mu}\sigma = \dot{\tau}_E - \mu\dot{\sigma}_E$, and by making use of equation

(1), the sliding velocity of the fault can be written as

$$\dot{v}(\xi,t) = F(v,\theta) = \frac{v}{a}\left[\frac{\dot{\tau}_E - \mu\dot{\sigma}_E}{\sigma} - \frac{b\dot{\theta}}{\theta}\right] . \tag{4}$$

The evolution of the state variable can simply be written as $\dot{\theta}(\xi,t) = H(v,\theta)$, since only the aging and slip laws are considered here and both state variable laws have the same linearization (e.g. *Ruina*, 1983). The nonlinear governing equations for $\dot{v}(\xi,t)$ and $\dot{\theta}(\xi,t)$ are now represented by the functions $F(v,\theta)$ and $H(v,\theta)$.

For quasi-static sliding, the changes in shear and normal stress are functions of the slip distribution $\delta(\xi,t)$, so that $\tau_E = T(\xi,\delta)$ and $\sigma_E = N(\xi,\delta)$. The functions $T(\xi,\delta)$ and $N(\xi,\delta)$ are the stress change functions mentioned in the Introduction. These functions must be determined by solving the appropriate 2D elasticity problem for a given fault geometry (see Appendix C for example) and contain all necessary information about the elastic response of the system. These functions also have the property that $\dot{\tau}_E = T(\xi,v)$ and $\dot{\sigma}_E = N(\xi,v)$ (e.g. *Viesca*, 2016a,b). Both $T(\xi,\delta)$ and $N(\xi,\delta)$ are equal to zero if there is no slip gradient.

Step 2. The uniform steady state of the system satisfies the conditions $F(v_0,\theta_0) = 0$ and $H(v_0,\theta_0) = 0$. Assume that the entire fault is sliding at steady state with velocity v_0, such that $T(\xi,v_0) = N(\xi,v_0) = 0$. For both the aging and slip laws, $H(v_0,\theta_0) = 0$ when $\theta_0 = d_c/v_0$. These conditions satisfy $F(v_0,\theta_0) = 0$, so the uniform steady state of the nonlinear system is $(v_0, d_c/v_0)$.

Step 3. To linearize the equations about the uniform steady state, first define

$$\mathbf{w}(\xi,t) = \begin{bmatrix} v(\xi,t) - v_0 \\ \theta(\xi,t) - \theta_0 \end{bmatrix} \tag{5}$$

where $\mathbf{w}(\xi,t)$ is a small perturbation away from (v_0,θ_0). Now the linearized equations can be written as $\dot{\mathbf{w}} = \boldsymbol{J}_0\mathbf{w}$. The Jacobian matrix $\boldsymbol{J}_0$ is most conveniently expressed in terms of the dimensionless variables: $\hat{t} = (v_0/d_c)t$, $\hat{v} = v/v_o$, and $\hat{\theta} = (v_0/d_c)\theta$, such that the uniform steady state becomes

$(\hat{v}_0, \hat{\theta}_0) = (1, 1)$. Then $\boldsymbol{J}_0$ can be written as

$$\boldsymbol{J}_0 = \begin{bmatrix} \frac{\partial \hat{F}_0}{\partial \hat{v}} & \frac{\partial \hat{F}_0}{\partial \hat{\theta}} \\ \\ \frac{\partial \hat{H}_0}{\partial \hat{v}} & \frac{\partial \hat{H}_0}{\partial \hat{\theta}} \end{bmatrix} = \begin{bmatrix} \left(\frac{b}{a}\right) \left[\frac{1}{b}(\hat{T}_{\hat{v}} - \mu_0 \hat{N}_{\hat{v}}) + 1\right] & \left(\frac{b}{a}\right) \boldsymbol{I} \\ \\ -\boldsymbol{I} & -\boldsymbol{I} \end{bmatrix} \tag{6}$$

where $\hat{F}_0 = \hat{F}(\hat{v}_0, \hat{\theta}_0)$, $\hat{H}_0 = \hat{H}(\hat{v}_0, \hat{\theta}_0)$, $\boldsymbol{I}$ is the identity matrix, and $\hat{T}_{\hat{v}}$ and $\hat{N}_{\hat{v}}$ denote derivatives with respect to $\hat{v}$. Some additional mathematical steps are provided in Appendix A. The dimensions of $\boldsymbol{J}_0$ will depend on whether the Jacobian is treated analytically or numerically.

Step 4. The eigenvalues and eigenvectors of $\boldsymbol{J}_0$ determine solutions to the linearized system ($\dot{\mathbf{w}} = \boldsymbol{J}_0 \mathbf{w}$) of the form $\mathbf{w}(\xi, t) \propto \boldsymbol{w}(k\xi)e^{pt}$. The eigenvectors $\boldsymbol{w}(k\xi)$ represent small spatial perturbations of wavenumber k to the uniform steady state. The eigenvalues p are the corresponding growth rates of those perturbations. If all of the eigenvalues of $\boldsymbol{J}_0$ have a negative real part then the system is linearly stable. If any eigenvalue has a positive real part then the system is linearly unstable (e.g. *Strogatz*, 2018).

3.1.1 Analytical Stability Analysis

For analytical results, $\boldsymbol{I} \rightarrow 1$ in equation (6) and $\boldsymbol{J}_0$ can be treated as a 2×2 matrix. Then the eigenvalues are found by solving the characteristic equation of $\boldsymbol{J}_0$, such that

$$p^2 + \left[1 - \tfrac{b}{a}(\Gamma + 1)\right] p - \left(\tfrac{b}{a}\right) \Gamma = 0 \; , \quad \Gamma = \tfrac{1}{b}(\hat{T}_{\hat{v}} - \mu_0 \hat{N}_{\hat{v}}) \; . \tag{7}$$

The eigenvalues do not need to be explicitly determined in cases where T_v and N_v are purely real functions. Instead, the stability of the system can be determined from conditions on $\det(\boldsymbol{J}_0) = -(b/a)\Gamma$ and $\mathrm{Tr}(\boldsymbol{J}_0) = (b/a)(\Gamma + 1) - 1$, where det() and Tr() denote the determinant and trace of the matrix, respectively. The system is unstable if either $\mathrm{Tr}(\boldsymbol{J}_0) > 0$, or $\det(\boldsymbol{J}_0) < 0$ (e.g. *Strogatz*, 2018, Figure 5.2.8); however, for all of the cases examined in this paper $\det(\boldsymbol{J}_0) > 0$. The trace instability condition can be written as

$$\left(\frac{b}{a}\right) \left[\frac{1}{b}(\hat{T}_{\hat{v}} - \mu_0 \hat{N}_{\hat{v}}) + 1\right] - 1 > 0 \; . \tag{8}$$

Equation (8) can be used to obtain analytical stability results. For example, in a spring-slider system $N_v = 0$ and $T_v = -K$, where K is the spring stiffness. Then solving equation (8) for K will yield the usual relation for the critical spring stiffness (see Appendix B.1).

For faults in a 2D medium, analytical results can be obtained by specifying the functional form of the spatial perturbation $\boldsymbol{w}(k\xi)$. For infinitely long faults there are no restrictions on the values of k because the fault has no boundaries. Then the general solution to the linear equations is

$$\mathbf{w}(\xi, t) = \int_{-\infty}^{\infty} A(k) \exp{(pt + ik\xi)} dk \ , \tag{9}$$

where $A(k)$ is determined by a Fourier transform of the initial conditions (*Pivato*, 2010). The steps of deriving equation (3) using equations (8) and (9) are detailed in Appendix B.2.

For a finite length fault with a uniform steady state velocity v_0, the sliding velocity must remain v_0 at the boundaries and so $\boldsymbol{w}(k\xi)$ must be equal to zero at the boundaries. If the fault is defined over $\xi = [0, L]$, the general solution to the linear equations that satisfies these boundary conditions is

$$\mathbf{w}(\xi, t) = \sum_n \boldsymbol{A}_n e^{pt} \sin(n\pi\xi/L) \ , \tag{10}$$

where the constants $\boldsymbol{A}_n$ are determined by Fourier series expansion of the initial conditions (*Pivato*, 2010). The allowable wavenumbers are $k = n\pi/L$ (for $n = 1, 2, ...$), analogous to the normal modes on a vibrating string. The possible values of k are discrete on a finite length fault and scaled by the fault length L, and this has important consequences for the stability behavior.

3.1.2 Numerical Stability Analysis

To conduct a linear stability analysis numerically, the fault can be discretized into n_e elements of length $d\xi$. Then $\boldsymbol{J}_0$ becomes a $2n_e \times 2n_e$ block matrix where in general the upper-left block $\partial \hat{F}_0/\partial \hat{v}$ is dense and the other blocks are sparse diagonal matrices. In discrete form, the functions $T(\xi, v)$ and $N(\xi, v)$ become linear operators on the slip velocity. For example, $T(\xi, v) \rightarrow \sum_{j=1}^{n_e} T_{ij} v_j$ and $T_v \rightarrow T_{ij}$, where T_{ij} is an $n_e \times n_e$ matrix and v_j is a vector of length n_e. All numerical results in this paper were obtained using a piecewise constant discretization of the stress change functions by assuming that slip is constant over regularly spaced elements along the fault.

The stability condition given by equation (8) is only valid for 2×2 matrices (e.g. *Luís*, 2021). The eigenvalues must be explicitly calculated for numerical analysis (e.g. *Viesca*, 2016a,b; *Ray and Viesca*, 2017; *Viesca*, 2023). The eigenvalues and eigenvectors can be directly computed using standard numerical routines; here the MATLAB functions *eig* and *eigs* are used. Numerically computing the eigenvalues will indicate if a fault system is stable or unstable for the specific set of RSF, elastic, and geometrical parameters that define the system. Determining the conditions (if any) where stability changes requires an iterative assessment of the stability for different parameter values. In this paper, critical fault lengths are determined using a bisection method to locate values of L where the stability changes (to within $\pm d\xi/2$) while other properties are held constant.

3.2 Nonlinear Simulations

In Section 4.2 the results of a limited set of simulations of the full nonlinear governing equations are presented to confirm some of the linear stability results. In these simulations the fault is loaded such that the steady state slip velocity along the entire fault is equal to $v_0 = 10^{-9}$ m/s. These simulations use the aging law for state variable evolution and rather than equation (1), use the regularized form of the rate and state friction equation (*Rice and Ben-Zion*, 1996; *Lapusta et al.*, 2000)

$$\mu(v,\theta) = a \sinh^{-1}\left[\frac{v}{2v_0}\exp\left(\frac{\mu_0 + b\ln(v_0\theta/d_c)}{a}\right)\right] . \tag{11}$$

In discrete form the stressing rate balance at the center of each fault element is

$$\dot{\mu}_i\sigma_i + \dot{\tau}_I = \sum_{j=1}^{n_e} T_{ij}(v_j - v_0) - \mu_i \sum_{j=1}^{n_e} N_{ij}(v_j - v_0) , \tag{12}$$

where $\dot{\mu}$ is found from equation (11) and $\dot{\tau}_I$ is the radiation damping approximation for the inertial stressing rate (*Rice*, 1993). The governing equations (12) with equation (11) and the aging law were solved along the entire length of the fault using a boundary element method implemented in MATLAB (see Data Availability statement for code availability).

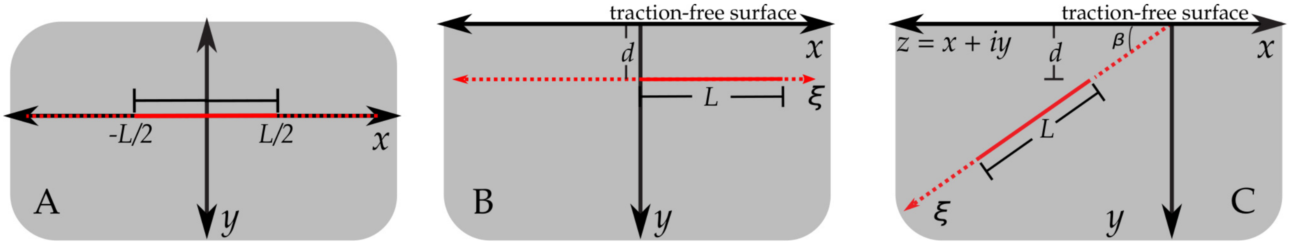

Figure 1: Diagrams of the fault system geometries used in this paper. In each panel a fault of length L is located by the solid red line; the dashed red line is the extension along the ξ-axis. **(A)** A fault in an infinite full-space, where the x- and ξ-axes coincide. **(B)** A fault at a depth d, parallel to a traction-free surface; both infinite and finite length systems are considered. **(C)** A fault dipping at an angle β relative to a traction-free surface, with its up-dip edge at a depth d. In panels B and C, the traction-free upper surface is defined by $y = 0$.

4 Results

Results are presented first for a finite length fault that is parallel to a traction-free surface, using a thin-layer approximation for the stress change functions. Analytical results are obtained for the thin-layer system, which provide insight into more complicated systems; numerical results for this system are presented as well. Next results are obtained numerically for vertical strike-slip faults, as well as faults in an infinite full-space. Finally, dip-slip faults of any orientation in a system with a traction-free surface are examined.

4.1 Thin Layer Approximation

Consider a fault of length L that is parallel to a traction-free surface at a depth d (Figure 1B). In general, this system will have a nonzero $N(\xi, v)$ for in-plane sliding (see Section 4.3). However, when $d \ll L_b = d_c G'/(b\sigma_0)$ then $N(\xi, v) = 0$ and the change in shear stress is (*Viesca*, 2016a)

$$T(\xi, v) = (dE')\frac{\partial^2 v}{\partial \xi^2} \ , \quad E' = \begin{cases} \frac{2G}{1-\nu}, & \text{in-plane sliding .} \\ G, & \text{anti-plane sliding .} \end{cases} \tag{13}$$

Note that equation (13) is a special case of the stress change function for a dipping fault geometry illustrated in Figure 1C, as described in Section 4.3. The critical wavelength for an infinitely long fault in this system is (*Viesca*, 2016b)

$$h_L^* = \frac{2\pi L_{bh}}{(1-a/b)^{1/2}} \,, \tag{14}$$

where $L_{bh} = \sqrt{dE' d_c/(b\sigma_0)}$ (see Appendix B.3.1).

Due to the simplicity of equation (13), analytical results for the critical fault length and the wavelengths of unstable modes can be obtained for finite length faults in this system. By assuming a solution for $v(\xi, t)$ of the form of equation (10), the normalized shear stress change function becomes $\hat{T}_{\hat{v}}/b = -(n\pi L_{\mathrm{bh}}/L)^2$ (see Appendix B.3.2 for details). Then via equation (8) the instability condition for the fault length becomes

$$L > \frac{n\pi L_{\mathrm{bh}}}{(1-a/b)^{1/2}} = \frac{n h_L^*}{2} \,. \tag{15}$$

Since the right hand side of equation (15) is smallest at $n = 1$, the critical fault length is

$$L_L^* = \frac{h_L^*}{2} \,. \tag{16}$$

Equation (16) indicates that the fault becomes unstable when it is long enough that the wavelength λ of the first mode ($n = 1$) of equation (10) becomes equal to $\lambda = 2\pi/k = 2L = h_L^*$.

The critical fault length L_L^* can also be numerically determined using the method described in Section 3.1.2. In this case by choosing a value of a/b then computing the stability of the system for different values of L. Then the critical fault length coincides with the value of L where the stability changes. Figure 2A displays the results of this process for nine different values of a/b and shows that the numerically determined values of L_L^* agree with equation (16).

As the fault length increases above L_L^*, progressively higher mode numbers will become unstable and the wavelength of the highest unstable mode number will approach h_L^* as $L \to \infty$. From equation (15), the total number of unstable modes that a fault can host is $n_T = \mathrm{Fl}(2L/h_L^*)$, where $\mathrm{Fl}(q)$ gives the greatest integer less than or equal to some quantity q. The wavelength of the highest mode number n_T is

$$\lambda_{n_T} = \frac{2L}{\mathrm{Fl}(2L/h_L^*)} \,, \quad \text{and} \quad \lim_{L\to\infty} \lambda_{n_T} = h_L^* \,. \tag{17}$$

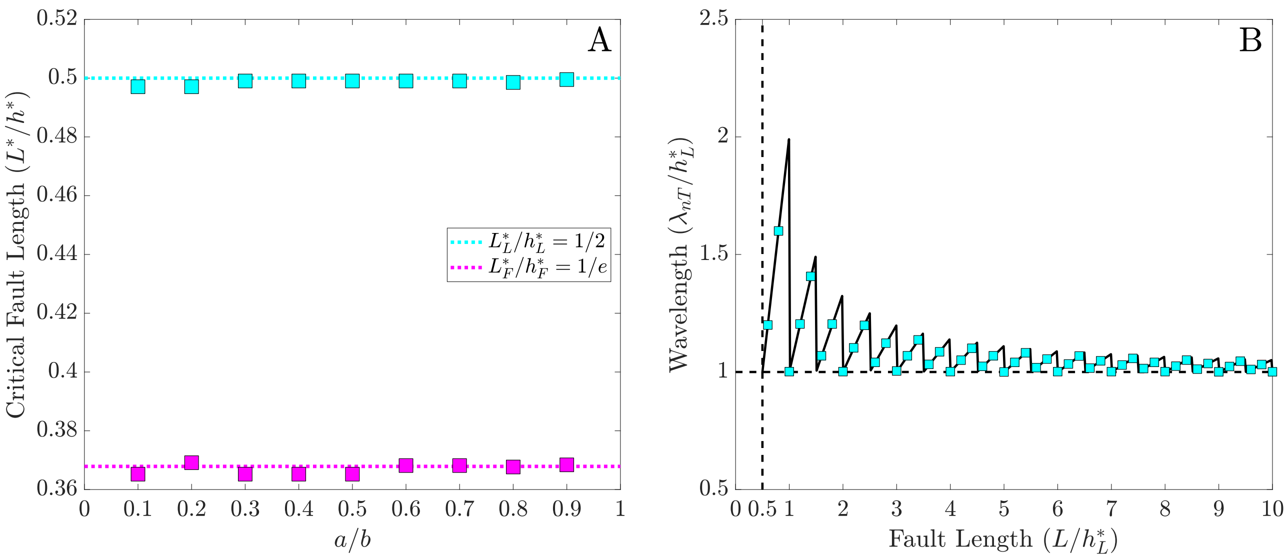

Figure 2: **(A)** Critical faults lengths L^* normalized by h_L^* for the thin layer (cyan) and by h_F^* for strike-slip/full-space (magenta) systems. The dotted lines correspond to expressions as shown in the legend; the squares are numerically determined boundaries as described in Section 3.1.2. Grid spacing for numerical calculations: $d\xi = L_b/80$ for full-space and $d\xi = L_{bh}/80$ for thin layer. **(B)** Wavelengths of the highest unstable mode number as a function of the fault length for the thin layer system, for $a/b = 0.5$. Both the wavelengths and the fault lengths are normalized by the critical wavelength h_L^*. The black line shows the analytical result given by equation (17), the cyan squares show the numerically determined wavelengths. For all calculations $L_b = 1600$ km; for thin layer calculations $d = 0.01L_b$.

Equation (17) predicts that $\lambda_{n_T} \geq h_L^*$ and approaches h_L^* with a type of saw-tooth pattern as $L \to \infty$ (Figure 2B). This result can also be confirmed numerically by computing the wavelength of the eigenvector for the highest unstable mode as a function of the fault length for $L > L_L^*$ (Figure 2B). The close agreement between the analytical and numerical analyses both validates the numerical method and confirms the behavior for finite length faults.

Another important consequence of finite fault length is that there is no minimum failure patch length required to generate an unstable sliding event for faults longer than L_L^*. Since equation (10) is a superposition of all mode numbers, instability will occur if any mode has a positive growth rate p. Thus, any set of initial conditions that gives $A_n \neq 0$ for an unstable mode will generate an instability; and there are no conditions on the length scale of the perturbation. This is illustrated further in the next section.

4.2 Vertical Strike-Slip Faults in a Half-Space and Full-Space Faults

Now consider a fault of length L embedded in a homogeneous full-space (Figure 1A). For this system $N(\xi, v) = 0$ and the change in shear stress is given by (e.g. *Segall*, 2010)

$$T(\xi, v) = \frac{G'}{2\pi} \int_{-L/2}^{L/2} \frac{\partial v/\partial s}{s - \xi} ds \; . \tag{18}$$

This stress change function is also valid for a vertical strike-slip fault in a half-space, in which case the integration is taken over $[d, d+L]$ and $G' = G$ (Figure 1C with $\beta = 90°$). Equation (18) takes the form of a Hilbert transform for an infinitely long fault ($L \to \infty$). Then the nucleation wavelength h^*_F given by equation (3) can be obtained from equation (8) after applying a Fourier transform (see Appendix B.2).

Analytical analysis using Fourier transforms cannot be applied to finite length faults due to the finite integration interval in equation (18). Instead, the stability analysis can be conducted numerically in the same manner as for the thin layer system, using the method described in Section 3.1.2. The results of the numerical stability analysis (Figure 2A) show that the critical fault length for the full-space system is

$$L^*_F \approx h^*_F/e \; . \tag{19}$$

Equation (19) is an approximate equality in the absence of analytical results. The scaling with e^{-1} is an interesting feature of equation (19) that emerges from the numerical linear stability analysis. A mathematical explanation for this scaling would require obtaining analytical results that in turn would require finding an exact or approximate solution to equation (18) after assuming a solution for $v(\xi, t)$ of the form of equation (10).

However, equation (19) is also supported by simulations of the full nonlinear governing equations following Section 3.2. Figure 3 shows the results of six sets of simulations using three values of a/b and two values of L_b. Nine simulations, each with a different fault length, were run for each pair of (a/b, L_b) values. In these simulations the initial conditions were set to the uniform steady state values, except for one element at the center of the fault where $v(\xi = 0, t = 0) = 0.99v_0$. Hence the spatial extent of the initial perturbation is as small as the numerical discretization allows. Three additional sets of simulations for $L_b = 1600$ km were conducted with the perturbation applied to a

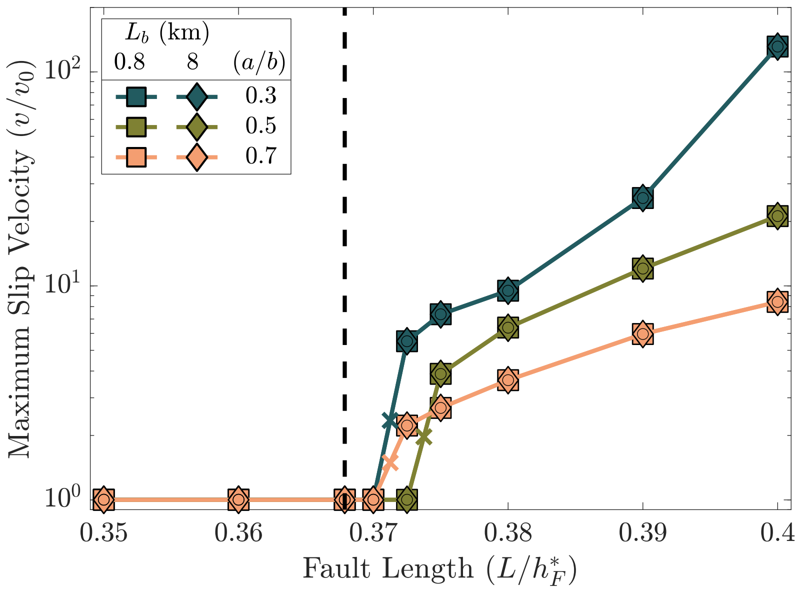

Figure 3: Normalized maximum slip velocities as a function of normalized fault length for faults in a full-space, or vertical strike-slip faults in a half-space. Colors correspond to values of a/b and symbols to values of L_b as indicated in the legend. Each symbol corresponds to an individual simulation. The squares and diamonds show results from simulations where a single numerical element at the center of the fault was perturbed; the circles show results where an element at the edge of the fault was perturbed. Note that the symbols overlie each other for each value of a/b, so there is no dependence on L_b or the location of the perturbation. The approximate critical fault lengths are marked by crosses and the vertical black, dashed line indicates $L/h_F^* = e^{-1}$. Grid spacing for simulations: $d\xi = L_b/80$.

single element at the edge of the fault.

The simulations were run until either consistent oscillations of maximum slip rate on the fault developed (i.e. a limit cycle), or the sliding velocity reached a uniform steady state such that $v(\xi, t) = v_0$. The critical fault length for each pair of (a/b, L_b) values lies in the interval of fault lengths that separate growth and decay of the initial perturbation, as indicated by the maximum slip velocity. These critical fault lengths (normalized by h_F^*) are 0.37125 ± 0.00125 for $a/b = 0.3, 0.7$ and 0.37375 ± 0.00125 for $a/b = 0.5$. There is no dependence on the value of L_b or the location of the perturbation (Figure 3). These critical fault lengths are within 2% of the value given by equation (19). Since the perturbation was restricted to a single fault element, these results also indicate that there is no minimum perturbation length scale.

4.3 Dip-Slip Faults

Consider in-plane sliding on a fault that is dipping at an angle β relative to the traction-free surface of a homogeneous, elastic half-space (Figure 1C). The up-dip edge of the fault is buried at a depth d below the traction-free surface. Both the full-space and parallel fault geometries are special cases of this dipping fault geometry. The full-space geometry is obtained when $d \to \infty$, and the parallel fault geometry is obtained when $d \neq 0$ and $\beta = 0$.

Stress change functions for the half-space geometry are available in the literature (*Dmowska and Kostrov*, 1973; *Freund and Barnett*, 1976; *Rudnicki and Wu*, 1995), and can be written as

$$T(\xi, v) = \int_{l}^{l+L} \Psi(z,\beta) \frac{\partial v}{\partial s} ds \;, \tag{20}$$

where $l = d/\sin(\beta)$, and $\Psi(z,\beta)$ is an analytic function of the complex variable $z = x+iy$ (*England*, 2003). A similar expression holds for $N(\xi, v)$. A derivation of these functions is presented in Appendix C. Note that these stress change functions are equivalent to using the *Okada* (1992) solutions for the middle of a very long dip-slip fault (e.g. *Liu and Rice*, 2007).

4.3.1 Velocity-Weakening Behavior

Critical fault lengths L_D^* for the dipping geometry can be determined by choosing a burial depth d and dip angle β and then conducting a numerical stability analysis as described in Section 3.1.2. Changing the value of L for fixed values of d and β corresponds to changing the down-dip depth of the fault. The stability calculation was repeated for dip angles in the range $\beta = 0° - 90°$ and burial depth values $d/h_F^* = 0$, 10^{-3}, 10^{-2}, 10^{-1}, 1 (the value $d = 0$ was omitted for $\beta = 0°$). This process was carried out for values of $\mu_0 = 0.2$, 0.6, 1, for both thrust and normal faults (Figure 4).

The critical fault length L_D^* approaches the full-space value given by equation (19) as $d \to h_F^*$. Therefore $L_D^* = L_F^*$ at depths $d \geq h_F^*$ and Figure 4 shows critical fault lengths for both thrust and normal faults in any possible orientation. For burial depths $d < h_F^*$, the critical fault length is approximately a log-linear function of d (Figure 5A).

The critical fault length L_D^* on the dip angle in a manner that is different for thrust and normal faults. There is also a secondary dependence on the value of μ_0 that depends on the sense of slip. For both thrust and normal faults, L_D^* increases with dip angle up to a value of $20° - 40°$, depending

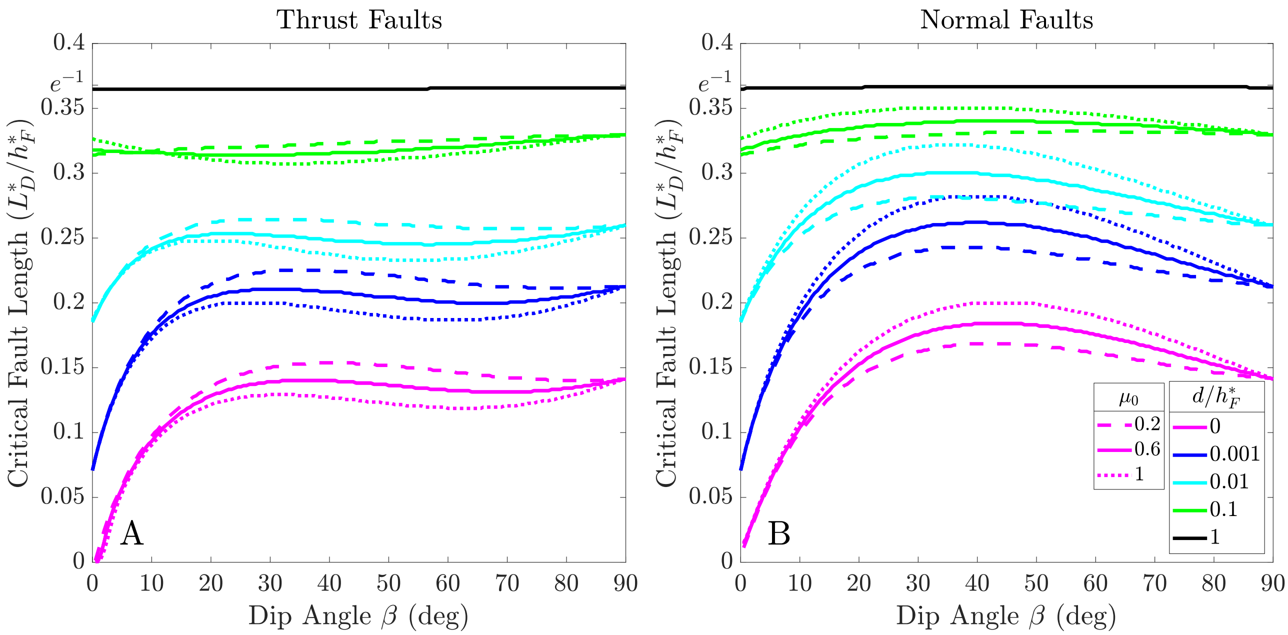

Figure 4: Critical fault lengths L_D^* for thrust and normal faults as a function of dip angle β, burial depth d, and friction coefficient μ_0. Critical fault lengths and burial depths are normalized by h_F^*. Values of d are indicated by colors, and values of μ_0 by line styles as indicated in the legend. Since the critical fault length can be very small, for these calculations the grid spacing was set to $d\xi = L_b/80$ or $d\xi = L/250$, whichever is smaller. The solid black lines are equal to e^{-1} to within 0.8%.

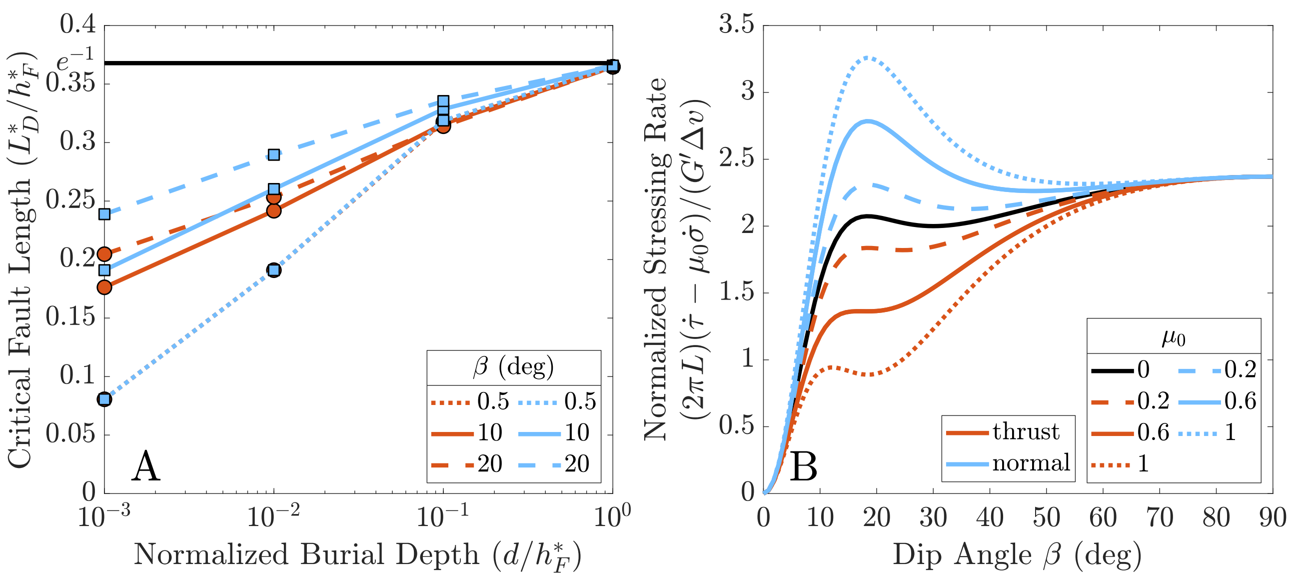

Figure 5: **(A)** Examples of critical fault lengths for thrust and normal faults as a function of burial depthfor $\beta = 0.5°$, $10°$, $20°$. **(B)** Normalized stressing rates $(2\pi L)(\dot{\tau}_E - \mu\dot{\sigma}_E)/(G'\Delta v)$ for thrust and normal faults. For both panels the sense of slip is indicated by colors as shown in the legend in panel B.

on the burial depth and sense of slip. For thrust faults, L_D^* then decreases to a secondary minimum before increasing again as $\beta \to 90°$. For normal faults, L_D^* reaches a maximum value then decreases as $\beta \to 90°$. Increasing the value of μ_0 decreases L_D^* for thrust faults, and does the opposite for normal faults. Values of L_D^* can become quite small on shallowly dipping faults that are near to the traction-free surface. In particular, as $\beta \to 0°$ on faults that break the surface ($d = 0$), $L_D^*/h_F^* \to 10^{-2}$ on normal faults and appears to approach zero on thrust faults.

The dependence of L_D^* on β and μ_0 can mostly be explained by considering the on-fault stressing rates due to a uniform slip velocity distribution Δv on a dipping fault of length L with burial depth $d = 0$. The elastic stressing rate on the fault is $\dot{\tau}_E - \mu\dot{\sigma}_E$ (see Section 3.1, Step 1), which can be computed by evaluating the stress change functions at the center of the fault $\xi = L/2$ (e.g. *Kato and Hirasawa*, 1997). The stressing rate has a dependence on β and μ_0 that shares some of the same features as that of L_D^*; including similar behavior as $\beta \to 0°$ and $\beta \to 90°$, and the same style of dependence on μ_0 for thrust and normal faults (Figure 5B).

The stressing rate calculation also provides an explanation for why values of L_D^* become very small at shallow dip angles. Sliding instability develops when the frictional weakening rate $\dot{\mu}$ is greater than the elastic stressing rate. The elastic stressing rate is approximately proportional to β/L for dip angles less than about $10°$ – $20°$ (Figure 5B). Then for a given set of frictional parameters, when the dip angle is small only shorter length faults can relieve elastic stress faster than the frictional weakening rate. This leads to the results displayed in Figure 4.

4.3.2 Velocity-Strengthening Behavior

As noted in the Introduction, it is possible for unstable behavior to occur on velocity-strengthening faults when a coupling between slip and normal stress exists, i.e. when $N(\xi, v) \neq 0$. The parameter space for the dipping fault geometry is large; the stability behavior can be expected to depend on frictional and elastic parameters μ_0, a/b, L_b; burial depth d; dip angle β; and fault length L. Additionally, while normalization by h_F^* accounts for dependence on RSF and elastic parameters for velocity-weakening behavior, h_F^* does not exist on velocity-strengthening faults. Therefore the results in this section are restricted to an infinitely long fault that is parallel to a traction-free surface, which reduces the parameter space to μ_0, a/b, and a normalized burial depth d/L_b. In this case equation (7) can be used to determine the stability of the system (see Appendix B.4 for stress

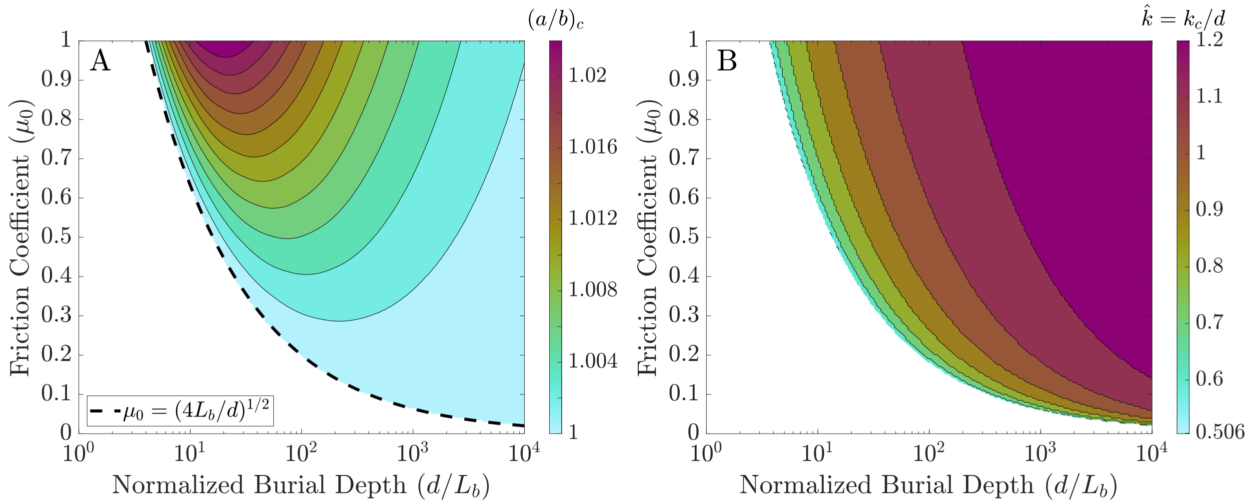

Figure 6: **(A)** Values of $(a/b)_c$, and **(B)** k_c/d for unstable behavior on infinitely long, velocity-strengthening faults near a traction-free surface, as a function of friction coefficient μ_0 and normalized burial depth d/L_b. The black, dashed line in **(A)** corresponds to the shallow stability boundary given by $d = (2/\mu_0)^2 L_b$.

change functions and details)

Figure 6 shows the results of choosing values of μ_0 and d/L_b, then determining the maximum value of $(a/b)_c = (a/b) > 1$ that satisfies $\mathrm{Re}(p) > 0$ in equation (7). One striking feature of the results is that unstable behavior only exists at depths greater than some minimum value that is very well approximated by

$$d = (2/\mu_0)^2 L_b \; . \tag{21}$$

The details of obtaining equation (21) are provided in Appendix B.4. At shallower depths there are no unstable solutions to equation (7) for $(a/b) > 1$. This shallow, stable region is not related to the thin layer limit that occurs at $d/L_b \ll 1$. Where unstable behavior occurs, for constant μ_0 there is depth at which $(a/b)_c$ reaches a maximum value. While for constant d/L_b, values of $(a/b)_c$ increase monotonically with μ_0, so the velocity-strengthening instability is enhanced when friction is higher.

An extensive parameter study to determine the effects of finite fault length and dip angle is beyond the scope of this study. However, some insight can by gained be examining the critical wavelengths that correspond to the values of $(a/b)_c$. Each value of $(a/b)_c$ shown in Figure 6A occurs at some critical wavenumber k_c that is in the neighborhood of $k_c/d \approx 1$ regardless of the value of $(a/b)_c$ (Figure 6B). By analogy with the velocity weakening results, if $L^* \approx h^*/e = 2\pi/(ek_c)$, then for any set of values $[\mu_0, (a/b)_c, d/L_b]$ taken from Figure 6A, the fault length would have to be

$L \geq 2\pi d/e$ for unstable behavior to occur.

5 Discussion

5.1 Some Theoretical Considerations

A main result in this paper is that the linear stability of frictional sliding depends on overall fault length. The critical fault length L^* can replace the concept of the critical nucleation length represented by h^*. Velocity-weakening faults are unstable if they are longer than L^*. In terms of linear behavior (where deviations from steady sliding are small), there is no minimum perturbation length scale that is needed to trigger an unstable sliding event if the fault length is longer than L^*. Velocity-weakening faults that are shorter than L^* should be considered conditionally stable, in that large perturbations out of the linear regime could generate unstable sliding events (e.g. *Gu et al.*, 1984). For vertical strike-slip faults $L^* \approx h^*_F/e$ (Section 4.2), while for dip-slip faults the critical fault length is a function of the dip angle and burial depth (Section 4.3). For sliding systems that can be treated as a thin layer (e.g. landslides, glaciers, or ice streams) $L^* = h^*_L/2$.

After nucleating, the details of how an instability develops (and any related length scales) depend on the nonlinear governing equations (*Rubin and Ampuero*, 2005, 2009; *Ampuero and Rubin*, 2008; *Viesca*, 2016a,b; *Ray and Viesca*, 2017; *Viesca*, 2023). As velocities increase towards inertially limited values on faults that obey the aging law, sliding localizes to patches with lengths that scale with L_b (e.g. *Rubin and Ampuero*, 2005; *Viesca*, 2016a). While for the slip law, *Viesca* (2023) showed that accelerating slip localizes towards a point, so that there is no minimum patch length. Together with the results in this paper, the implication is that there is no nucleation length scale on faults that obey the slip law. This could be important, considering that recent work has shown that the slip law can explain a wider range of experimental observations than the aging law (*Bhattacharya et al.*, 2015, 2017, 2022).

However, all of the results in this paper rely on idealized fault systems that do not include multiple interacting faults; heterogeneous frictional and material properties; non-uniform steady state conditions; or inelastic deformation. It is possible that examining more realistic finite length fault systems may lead to different conclusions regarding nucleation length scales. In addition, the results also represent the idealizations that are incorporated into the RSF equations as they are applied to laboratory experiments. The RSF equations, including the multiple different state evolution laws, have all been determined through application of spring-slider models to experimental data (*Dieterich*, 1979; *Ruina*, 1983). Thus the possible effects of traction-free surfaces (which are numerous in most experimental geometries) on laboratory frictional behavior is mostly unknown (*Aldam et al.*, 2016).

Finally, it is clear that when examining heterogeneous systems, the fault system must be treated as a single entity. For example, applying the critical nucleation length from equation (3) to the velocity-weakening sections of a dipping fault that also has velocity-strengthening sections will result in inaccurate assessments of sliding stability. The stability behavior will instead depend on the geometrical aspects as well as the frictional properties in both the velocity-weakening and -strengthening portions of the fault (*Skarbek et al.*, 2012; *Dublanchet et al.*, 2013; *Ray and Viesca*, 2017; *Yabe and Ide*, 2017; *Luo and Ampuero*, 2018).

5.2 Some Practical Considerations

Proximity to a traction-free surface, as measured by h^*_F or L_b, has a significant influence on stability properties. Since both h^*_F and L_b are inversely proportional to effective normal stress, the normalized burial depths in Figures 4 and 6 are smaller on faults with high pore fluid pressure. This means that the influence of the free surface is enhanced on overpressured fault systems. High pore pressure leads to smaller normalized critical fault lengths, but larger values of h^*_F. If the burial depth is less than h^*_F, then the free surface will influence the stability behavior. This effect should for example be important in the shallow regions of subduction zones and in areas of induced seismicity where pore pressures can be elevated. Particularly on subduction megathrust plate boundaries, the combination of shallow dip angles and high pore pressures should lead to very small normalized critical fault lengths.

The effect of shallow burial depth on unstable behavior for velocity-strengthening faults is more complicated. A parallel fault should be the most unstable geometry for a nonzero burial depth d, since on a dipping fault the depth from the traction-free surface will increase with down-dip distance. The values of $(a/b)_c$ for the infinite fault system in Figure 6A are close to velocity-neutral, so it seems reasonable to assume that values of $(a/b)_c$ would be even closer to unity on finite length, dipping faults that are buried. However, the velocity-weakening results show that intersecting the free surface causes a significant reduction in stability; L_D^*/h_F^* decreases logarithmically with decreasing d/h_F^*. So it is possible that values of $(a/b)_c$ may be larger on dipping faults where $d = 0$. Certainly more work is needed to understand this behavior.

Multiple effects have been described that can cause unstable sliding on velocity-strengthening faults: contrasting elastic parameters across a fault (*Rice et al.*, 2001; *Ranjith*, 2014); poroelasticity (*Heimisson et al.*, 2019); "fault valve" behavior (*Ozawa et al.*, 2024); and proximity to a traction-free surface (this paper; *Aldam et al.*, 2016). All of these features are commonplace in fault systems as well as in other frictional systems like landslides and ice streams. For example, all of these effects could be present in the shallow regions of subduction zones and may contribute towards enabling shallow slow slip events (e.g. *Saffer and Wallace*, 2015), or influencing the behavior of tsunami earthquakes (e.g. *Bilek and Lay*, 2002).

6 Conclusion

The results in this paper show how even simple types of geometrical complexity can change stability behavior. Using numerical methods makes it possible to conduct linear stability analyses for a wide range of fault systems that cannot be examined using analytical techniques. Some examples of systems for which stress change functions are available in the literature are multi-fault systems and non-planer faults in a 3D homogeneous elastic half-space (*Okada*, 1992; *Meade*, 2007). Functions are also available for different types of viscoelastic geometries (*Segall*, 2010; *Lambert and Barbot*, 2016, e.g.). Heterogeneous on-fault frictional properties can be used with any existing stress change functions (e.g. *Ray and Viesca*, 2017). Finally, numerical stability methods could also be extended to include dilatancy and changes in pore pressure, or other types of frictional constitutive behavior (e.g. *Segall and Rice*, 1995; *Chen and Spiers*, 2016; *Barbot*, 2022).

Data Availability

All of the calculations and figures in this paper can be reproduced using a MATLAB package *RS-FaultZ* available at `https://github.com/rmskarbek/RSFaultZ` (*Skarbek*, 2024). The m-files for automatically generating figures are stored in the github repository directory: RSFaultZ/examples/stability.

Acknowledgments

This work was supported by the National Science Foundation under Grant No. EAR-2245540. The author thanks D. Saffer, H. Savage, and R. Viesca for discussions that helped and influenced this paper. Colors for Figure 6 were generated using a perceptually uniform color map (*Crameri*, 2019; *Crameri et al.*, 2020).

References

Aldam, M., Y. Bar-Sinai, I. Svetlizky, E. A. Brener, J. Fineberg, and E. Bouchbinder (2016), Frictional sliding without geometrical reflection symmetry, *Phys. Rev. X*, *6*, 041,023, doi:10.1103/PhysRevX.6.041023.

Aldam, M., M. Weikamp, R. Spatschek, E. A. Brener, and E. Bouchbinder (2017), Critical nucleation length for accelerating frictional slip, *Geophys. Res. Lett.*, *44*(22), 11,390–11,398, doi:https://doi.org/10.1002/2017GL074939.

Ampuero, J.-P., and A. M. Rubin (2008), Earthquake nucleation on rate and state faults - Aging and slip laws, *J. Geophys. Res.*, *113*, B01302, doi:10.1029/2007JB005082.

Barbot, S. (2022), A rate-, state-, and temperature-dependent friction law with competing healing mechanisms, *J. Geophys. Res.*, *127*(11), e2022JB025,106, doi:https://doi.org/10.1029/2022JB025106.

Bhattacharya, P., A. M. Rubin, E. Bayart, H. M. Savage, and C. Marone (2015), Critical evaluation of state evolution laws in rate and state friction: Fitting large velocity steps in simulated fault gouge with time-, slip-, and stress-dependent constitutive laws, *J. Geophys. Res.*, *120*(9), 6365–6385, doi:10.1002/2015JB012437.

Bhattacharya, P., A. M. Rubin, and N. M. Beeler (2017), Does fault strengthening in laboratory rock friction experiments really depend primarily upon time and not slip?, *J. Geophys. Res.*, *122*(8), 6389–6430, doi:10.1002/2017JB013936.

Bhattacharya, P., A. M. Rubin, T. E. Tullis, N. M. Beeler, and K. Okazaki (2022), The evolution of rock friction is more sensitive to slip than elapsed time, even at near-zero slip rates, *Proc. Natl. Acad. Sci. U. S. A.*, *119*(30), e2119462,119, doi:10.1073/pnas.2119462119.

Bilek, S. L., and T. Lay (2002), Tsunami earthquakes possibly widespread manifestations of frictional conditional stability, *Geophys. Res. Lett.*, *29*(14), 18–1–18–4, doi:10.1029/2002GL015215.

Bindschadler, R. A., M. A. King, R. B. Alley, S. Anandakrishnan, and L. Padman (2003), Tidally controlled stick-slip discharge of a west antarctic ice, *Science*, *301*(5636), 1087–1089, doi:10.1126/science.1087231.

Bower, A. F. (2009), *Applied mechanics of solids*, CRC press.

Bürgmann, R. (2018), The geophysics, geology and mechanics of slow fault slip, *Earth Planet. Sci. Lett.*, *495*, 112 – 134, doi:https://doi.org/10.1016/j.epsl.2018.04.062.

Chen, J., and C. J. Spiers (2016), Rate and state frictional and healing behavior of carbonate fault gouge explained using microphysical model, *J. Geophy. Res.*, *121*(12), 8642–8665, doi:https://doi.org/10.1002/2016JB013470.

Crameri, F. (2019), Scientific colour maps, doi:10.5281/ZENODO.1243862.

Crameri, F., G. E. Shephard, and P. J. Heron (2020), The misuse of colour in science communication, *Nature communications*, *11*(1), 5444, doi:https://doi.org/10.1038/s41467-020-19160-7.

Dieterich, J. H. (1979), Modeling of rock friction: 1. Experimental results and constitutive equations, *J. Geophys. Res.*, *84*(B5), 2161–2168, doi:10.1029/JB084iB05p02161.

Dieterich, J. H. (1992), Earthquake nucleation on faults with rate- and state-dependent strength, *Tectonophysics*, *211*(1-4), 115–134, doi:10.1016/0040-1951(92)90055-B.

Dmowska, R., and B. V. Kostrov (1973), A shear crack in a semi-space under plane strain conditions, *Archives of Mechanics*, *25*(3), 421 – 440.

Dublanchet, P., P. Bernard, and P. Favreau (2013), Interactions and triggering in a 3-d rate-and-state asperity model, *J. Geophys. Res.*, *118*(5), 2225–2245, doi:https://doi.org/10.1002/jgrb.50187.

England, A. H. (2003), *Complex variable methods in elasticity*, Courier Corporation.

Freund, L. B., and D. M. Barnett (1976), A two-dimensional analysis of surface deformation due to dip-slip faulting, *Bull. Seismol. Soc. Am.*, *66*(3), 667, errata, Bull. Seismol. Soc. Am., 66, 2083-2084, 1976.

Gu, J.-C., J. R. Rice, A. L. Ruina, and S. T. Tse (1984), Slip motion and stability of a single degree of freedom elastic system with rate and state dependent friction, *Jourxnal of the Mechanics and Physics of Solids*, *32*(3), 167 – 196, doi:https://doi.org/10.1016/0022-5096(84)90007-3.

Handwerger, A. L., A. W. Rempel, R. M. Skarbek, J. J. Roering, and G. Hilley (2016), Rate-weakening friction characterizes both slow sliding and catastrophic failure of landslides, *Proc. Natl. Acad. Sci. U.S.A.*, *113*(37), 10,281–10,286, doi:10.1073/pnas.1607009113.

Heimisson, E. R., E. M. Dunham, and M. Almquist (2019), Poroelastic effects destabilize mildly rate-strengthening friction to generate stable slow slip pulses, *J. Mech. Phys. Solids*, *130*, 262 – 279, doi:https://doi.org/10.1016/j.jmps.2019.06.007.

Horowitz, F. G., and A. Ruina (1989), Slip patterns in a spatially homogeneous fault model, *J. Geophys. Res.*, *94*(B8), 10,279–10,298, doi:https://doi.org/10.1029/JB094iB08p10279.

Kato, N., and T. Hirasawa (1997), A numerical study on seismic coupling along subduction zones using a laboratory-derived friction law, *Phys. Earth Planet. Inter.*, *102*(1), 51–68, doi:https://doi.org/10.1016/S0031-9201(96)03264-5.

Lambert, V., and S. Barbot (2016), Contribution of viscoelastic flow in earthquake cycles within the lithosphere-asthenosphere system, *Geophys. Res. Lett.*, *43*(19), 10,142–10,154, doi:https://doi.org/10.1002/2016GL070345.

Lapusta, N., J. R. Rice, Y. Ben-Zion, and G. Zheng (2000), Elastodynamic analysis for slow tectonic loading with spontaneous rupture episodes on faults with rate-and-state dependent friction, *J. Geophys. Res.*, *105*(B10), 23,765–23,789, doi:10.1029/2000JB900250.

Lipovsky, B. P., and E. M. Dunham (2017), Slow-slip events on the whillans ice plain, antarctica, described using rate-and-state friction as an ice stream sliding law, *J. Geophys. Res.*, *122*(4), 973–1003, doi:https://doi.org/10.1002/2016JF004183.

Liu, Y., and J. R. Rice (2007), Spontaneous and triggered aseismic deformation transients in a subduction fault model, *J. Geophys. Res.*, *112*, B09404, doi:10.1029/2007jb004930.

Luís, R. (2021), Linear stability conditions for a first order n-dimensional mapping, *Qualitative theory of dynamical systems*, *20*(1), 20, doi:https://doi.org/10.1007/s12346-021-00455-z.

Luo, Y., and J.-P. Ampuero (2018), Stability of faults with heterogeneous friction properties and effective normal stress, *Tectonophysics*, *733*, 257–272, doi:https://doi.org/10.1016/j.tecto.2017.11.006.

Marone, C. (1998), Laboratory-derived friction laws and their application to seismic faulting, *Annu. Rev. Earth Planet. Sci.*, *26*, 643–696, doi:10.1146/annurev.earth.26.1.643.

Meade, B. J. (2007), Algorithms for the calculation of exact displacements, strains, and stresses for triangular dislocation elements in a uniform elastic half space, *Computers & Geosciences*, *33*(8), 1064–1075, doi:https://doi.org/10.1016/j.cageo.2006.12.003.

Okada, Y. (1992), Internal deformation due to shear and tensile faults in a half-space, *Bull. Seismol. Soc. Am.*, *82*(2), 1018.

Ozawa, S., Y. Yang, and E. M. Dunham (2024), Fault-valve instability: A mechanism for slow slip events, *ESS Open Archive*, doi:10.22541/essoar.171291623.31088922/v1.

Pivato, M. (2010), *Linear Partial Differential Equations and Fourier Theory*, Cambridge University Press, doi:10.1017/CBO9780511810183.

Ranjith, K. (2014), Instabilities in dynamic anti-plane sliding of an elastic layer on a dissimilar elastic half-space, *Journal of Elasticity*, *115*(1), 47–59, doi:10.1007/s10659-013-9446-1.

Ray, S., and R. C. Viesca (2017), Earthquake nucleation on faults with heterogeneous frictional properties, normal stress, *J. Geophys. Res.*, *122*(10), 8214–8240, doi:10.1002/2017JB014521.

Rice, J., and A. L. Ruina (1983), Stability of steady frictional slipping, *Journal of applied mechanics*, *50*(2), 343–349, doi:10.1115/1.3167042.

Rice, J. R. (1993), Spatiotemporal complexity of slip on a fault, *J. Geophys. Res.*, *98*(B6), 9885–9907, doi:10.1029/93JB00191.

Rice, J. R., and Y. Ben-Zion (1996), Slip complexity in earthquake fault models., *Proc. Natl. Acad. Sci. U.S.A.*, *93*(9), 3811–3818, doi:10.1073/pnas.93.9.3811.

Rice, J. R., N. Lapusta, and K. Ranjith (2001), Rate and state dependent friction and the stability of sliding between elastically deformable solids, *Journal of the Mechanics and Physics of Solids*, *49*(9), 1865 – 1898, doi:http://dx.doi.org/10.1016/S0022-5096(01)00042-4.

Rubin, A. M., and J.-P. Ampuero (2005), Earthquake nucleation on (ageing) rate and state faults, *J. Geophys. Res.*, *110*, B11312, doi:10.1029/2005JB003686.

Rubin, A. M., and J.-P. Ampuero (2009), Self-similar slip pulses during rate-and-state earthquake nucleation, *J. Geophys. Res.*, *114*(B11), doi:https://doi.org/10.1029/2009jb006529.

Rudnicki, J. W., and M. Wu (1995), Mechanics of dip-slip faulting in an elastic half-space, *J. Geophys. Res.*, *100*(B11), 22,173–22,186, doi:https://doi.org/10.1029/95JB02246.

Ruina, A. (1983), Slip instability and state variable friction laws, *J. Geophys. Res.*, *88*, 10,359–10,370.

Saffer, D. M., and L. M. Wallace (2015), The frictional, hydrologic, metamorphic and thermal habitat of shallow slow earthquakes, *Nat. Geosc.*, *8*, 594 – 600, doi:10.1038/ngeo2490.

Scholz, C. H. (2019), *The Mechanics of Earthquakes and Faulting*, Cambridge University Press, Singapore.

Schwartz, S. Y., and J. M. Rokosky (2007), Slow slip events and seismic tremor at circum-pacific subduction zones, *Rev. Geophys.*, *45*(3), doi:10.1029/2006RG000208.

Segall, P. (2010), *Earthquake and Volcano Deformation*, 424 pp., Princeton Univ. Press, Princeton, N.J.

Segall, P., and J. R. Rice (1995), Dilatancy, compaction, and slip instability of a fluid infiltrated fault, *J. Geophys. Res.*, *100*, 22,155–22,171.

Skarbek, R. M. (2024), rmskarbek/RSFaultZ: v1.0, doi:10.5281/zenodo.10497312.

Skarbek, R. M., A. W. Rempel, and D. A. Schmidt (2012), Geologic heterogeneity can produce aseismic slip transients, *Geophys. Res. Lett.*, *39*(21), doi:10.1029/2012GL053762.

Strogatz, S. H. (2018), *Nonlinear dynamics and chaos with student solutions manual: With applications to physics, biology, chemistry, and engineering*, CRC press, doi:https://doi.org/10.1201/9780429492563.

Uenishi, K., and J. R. Rice (2003), Universal nucleation length for slip-weakening rupture instability under nonuniform fault loading, *J. Geophys. Res.*, *108*(B1), doi:https://doi.org/10.1029/2001JB001681.

Viesca, R. C. (2016a), Stable and unstable development of an interfacial sliding instability, *Phys. Rev. E*, *93*, 060,202, doi:10.1103/PhysRevE.93.060202.

Viesca, R. C. (2016b), Self-similar slip instability on interfaces with rate- and state-dependent friction, *Proc. R. Soc. A*, *472*(2192), doi:10.1098/rspa.2016.0254.

Viesca, R. C. (2023), Frictional state evolution laws and the non-linear nucleation of dynamic shear rupture, *J. Mech. Phys. Solids*, *173*, 105,221, doi:https://doi.org/10.1016/j.jmps.2023.105221.

Weertman, J. (1996), *Dislocation Based Fracture Mechanics*, World Scientific, doi:10.1142/3062.

Yabe, S., and S. Ide (2017), Slip-behavior transitions of a heterogeneous linear fault, *J. Geophys. Res.*, *122*(1), 387–410, doi:https://doi.org/10.1002/2016JB013132.

Zoet, L. K., M. J. Ikari, R. B. Alley, C. Marone, S. Anandakrishnan, B. M. Carpenter, and M. M. Scuderi (2020), Application of constitutive friction laws to glacier seismicity, *Geophysical Research Letters*, *47*(21), e2020GL088,964, doi:https://doi.org/10.1029/2020GL088964, e2020GL088964 2020GL088964.

Appendix A Linearization of RSF Equations

Additional mathematical details are provided here for obtaining the Jacobian matrix given by equation (6). First, using equations (2) and (4), the linearized equations can be written as

$$\dot{v} = \left(\frac{\partial F_0}{\partial v}\right) v + \left(\frac{\partial F_0}{\partial \theta}\right) \theta = \left(\frac{v_0}{a}\right) \left[\frac{1}{\sigma_0}\left(\frac{\partial \dot{\tau}_E}{\partial v} - \mu_0 \frac{\partial \dot{\sigma}_E}{\partial v}\right) + \frac{b}{d_c}\right] v + \left(\frac{b v_0^3}{a d_c^2}\right) \theta \ , \tag{A1}$$

and

$$\dot{\theta} = \left(\frac{\partial H_0}{\partial v}\right) v + \left(\frac{\partial H_0}{\partial \theta}\right) \theta = -\left(\frac{1}{v_0}\right) v - \left(\frac{v_0}{d_c}\right) \theta \ . \tag{A2}$$

Equations (A1) and (A2) can be used to define a dimensional Jacobian. The elements of equation (6) are obtained after changing to the dimensionless variables defined by $\hat{t} = (v_0/d_c)t$, $\hat{v} = v/v_o$, and $\hat{\theta} = (v_0/d_c)\theta$. Dimensionless stress change functions are obtained by normalizing stresses by σ_0. So for example, $\dot{\tau}_E = T(\xi, v) = (\sigma_0 v_0/d_c)\hat{T}$.

Appendix B Analytical Linear Stability Results

B.1 Spring-Slider

The shear stress change in the basic spring-slider model is

$$\dot{\tau}_E = K(v_0 - v) \ , \tag{B1}$$

where K is a normalized spring stiffness with units of [Stress / Length]. Using the same dimensionless variables defined in A, the dimensionless shear stress change function is

$$\hat{T}(\hat{v}) = \frac{d_c K}{\sigma_0}(1 - \hat{v}) \ . \tag{B2}$$

Inserting the derivative of equation (B2) with respect to $\hat{v}$ into equation (8) and setting the left-hand side equal to zero yields the critical stiffness $K_c = \sigma_0(b - a)/d_c$.

B.2 Infinite Fault in a Full-Space

For infinite faults the critical wavelength can be found by searching for solutions of the form $v(\xi,t) = A\exp(pt + ik\xi)$. For a full-space, the shear stress change function can be found by substituting this expression into equation (18), for $L \to \infty$; this is essentially the method used by (*Rice et al.*, 2001):

$$T(\xi, v) = ikA\left(\frac{G'}{2\pi}\right)\int_{-\infty}^{\infty}\frac{\exp(pt+iks)}{s-\xi}ds\ . \tag{B3}$$

After making a change of variables $u = s - \xi$, equation (B3) becomes

$$\begin{aligned} T(\xi, v) &= ik\left(\frac{G'}{2\pi}\right)A\exp(pt+ik\xi)\int_{-\infty}^{\infty}\frac{\exp(iku)}{u}du \\ &= -\left(\frac{|k|G'}{2}\right)v\ , \end{aligned} \tag{B4}$$

where the integral in the first line is a Fourier Transform of $1/u$ and is equal to $i\pi\text{sgn}(k)$. Using the previously defined dimensionless variables, but leaving k in dimensional form, the critical wavenumber k_c from equation (8) is

$$\left(\frac{b}{a}\right)\left(1 - \frac{L_b|k_c|}{2}\right) - 1 = 0\ , \tag{B5}$$

which leads to equation (3) since the critical wavelength is defined as $h_F^* = \lambda_c = 2\pi/k_c$.

B.3 Thin Layer

B.3.1 Infinite fault

The critical wavelength for the thin layer system can be found by following the same procedure for the full-space system, but using equation (13) for the shear stress change function.

$$T(\xi, v) = (dE')\frac{\partial^2}{\partial\xi^2}[A\exp(pt+ik\xi)] = -dE'k^2v\ . \tag{B6}$$

Using the dimensionless variables as before, equation (8) becomes

$$\left(\frac{b}{a}\right)\left[1 - (L_{bh}k_c)^2\right] - 1 = 0\ , \tag{B7}$$

with $L_{bh} = \sqrt{dE' d_c/(b\sigma_0)}$ (*Viesca*, 2016b). Solving equation (B7) for the critical wavelength leads to equation (14) for h^*_L.

B.3.2 Finite Fault

For a finite fault the deviation of the sliding velocity from steady state takes the form $v(\xi, t) - v_0 = a_n e^{pt} \sin(n\pi\xi/L)$. After substituting this into equation (13), the shear stress change becomes

$$T(\xi, v) = -dE' \left(\frac{n\pi}{L}\right)^2 a_n e^{pt} \sin(n\pi\xi/L) = -dE' \left(\frac{n\pi}{L}\right)^2 v \ , \tag{B8}$$

such that

$$T_v = \frac{\partial}{\partial v} T(\xi, v) = -dE' \left(\frac{n\pi}{L}\right)^2 \ . \tag{B9}$$

Equation (B9) can be normalized using the dimensionless quantities defined in Appendix A and remembering that T has units of [stress/time], then

$$\frac{\hat{T}_{\hat{v}}}{b} = -\left(\frac{n\pi L_{\mathrm{bh}}}{L}\right)^2 \ , \tag{B10}$$

as in Section 4.1. Finally, the critical fault length is obtained by substituting equation (B10) into equation (8), which yields equation (15).

B.4 Velocity-Strengthening Layer

The stress change functions for in-plane sliding on an infinitely long fault that is parallel to a traction-free surface at a depth d are (e.g. *Viesca*, 2016a)

$$T(\xi, v) = \frac{G}{2\pi(1-\nu)} \int_{-\infty}^{\infty} \left\{ \frac{1}{s-\xi} - \frac{s-\xi}{4d^2 + (s-\xi)^2} + \frac{8d^2(s-\xi)}{[4d^2 + (s-\xi)^2]^2} \right.$$
$$\left. + \frac{4d^2(s-\xi)^3 - 48d^4(s-\xi)}{[4d^2 + (s-\xi)^2]^3} \right\} \frac{\partial v}{\partial s} ds \ , \tag{B11}$$

and

$$N(\xi, v) = \frac{G}{2\pi(1-\nu)} \int_{-\infty}^{\infty} \left\{ \frac{32d^5 - 24d^3(s-\xi)^2}{[4d^2 + (s-\xi)^2]^3} \right\} \frac{\partial v}{\partial s} ds \ . \tag{B12}$$

The stability of this system is most easily determined after applying a Fourier transform. Using the Fourier transform pair:

$$\tilde{f}(k) = F[f(x)] = \int_{-\infty}^{\infty} f(x) e^{-ikx} dx \tag{B13}$$

$$f(x) = F^{-1}[\tilde{f}(k)] = \frac{1}{2\pi} \int_{-\infty}^{\infty} \tilde{f}(k) e^{ikx} dx \ , \tag{B14}$$

equations (B11) and (B12) become

$$\widetilde{T}(k, \tilde{v}) = -\left(\frac{G'|k|}{2}\right) \left\{1 - e^{-2d|k|}\left[1 - 2d|k| + 2(dk)^2\right]\right\} \tilde{v} \ , \tag{B15}$$

and

$$\widetilde{N}(k, \tilde{v}) = -iG'k(dk)^2 e^{-2d|k|} \tilde{v} \ . \tag{B16}$$

where tildes denote transformed quantities. Note that these functions are provided by *Viesca* (2016a) using a different transform pair.

The eigenvalues p can then be computed from equation (7) after defining $\Gamma = (1/b)(\widetilde{T}_{\tilde{v}} - \mu_0 \widetilde{N}_{\tilde{v}})$ using equations (B15) and (B16). Using the dimensionless variables, and also defining $\hat{k} = dk$ yields

$$\Gamma = -\left(\frac{L_b}{d}\right) \left\{\frac{|\hat{k}|}{2}\left[1 - e^{-2|\hat{k}|}\left(1 - 2|\hat{k}| + 2\hat{k}^2\right)\right] - i\mu_0 \hat{k}^3 e^{-2\hat{k}}\right\} \ . \tag{B17}$$

The resulting equation for p is complex and depends on the values of (a/b), (L_b/d), μ_0, and the dimensionless wavenumber $\hat{k}$. The results in Figure 6 were obtained through an iterative process by solving for p numerically as a function of $\hat{k}$ for chosen values of L_b/d and μ_0. For each pair of values $(L_b/d, \mu_0)$, $p(\hat{k})$ was first determined for a value of $(a/b) < 1$, which guarantees that $\text{Re}[p(\hat{k})] > 0$ for some value of $\hat{k}$; numerical tests showed that the maximum value of $p(\hat{k})$ occurs in the vicinity of $\hat{k} \approx 1$. This process was then repeated for incrementally larger values of (a/b) until $\text{Re}[p(\hat{k})] < 0$ for all values of $\hat{k}$, which determines the values of $(a/b)_c$ shown in Figure 6A.

The minimum depth for unstable behavior can be approximately determined by solving for p for a specific value of $\hat{k}$. From the results in Figure 6B, the stability boundary occurs at $\hat{k} \approx 0.5$, so that

$$\Gamma = -\left(\frac{L_b}{d}\right)\left[\left(\frac{2-e^{-1}}{8}\right) - i\mu_0\left(\frac{e^{-1}}{8}\right)\right] . \tag{B18}$$

Additionally, that stability boundary occurs at $(a/b) = 1$. With these values of $\hat{k}$ and (a/b), equation (7) becomes

$$p^2 - \left(\frac{L_b}{d}\right)\left[\left(\frac{2-e^{-1}}{8}\right) - i\mu_0\left(\frac{e^{-1}}{8}\right)\right] p + \left(\frac{L_b}{d}\right)\left[\left(\frac{2-e^{-1}}{8}\right) - i\mu_0\left(\frac{e^{-1}}{8}\right)\right] = 0 . \tag{B19}$$

Now p can be solved for using a procedure described in *Rice et al.* (2001). First, Figure 6 indicates that for a constant value of μ_0, the real part of p changes sign as d/L_b increases from zero. The sign change occurs at $p = i\rho$; substituting this into equation (B19) yields

$$\left[-\rho^2 - \left(\frac{\mu_0 e^{-1} L_b}{8d}\right)\rho + \frac{(2-e^{-1})L_b}{8d}\right] - i\left(\frac{L_b}{d}\right)\left[\left(\frac{2-e^{-1}}{8}\right)\rho + \frac{\mu_0 e^{-1}}{8}\right] = 0 . \tag{B20}$$

Equation (B20) is satisfied when both its real and imaginary parts are equal to zero. Setting the real part equal to zero provides an equation for ρ in terms of μ_0 and (L_b/d):

$$\rho = -\left(\frac{\mu_0 e^{-1} L_b}{16d}\right) \pm \frac{1}{2}\sqrt{\left(\frac{\mu_0 e^{-1} L_b}{8d}\right)^2 - \frac{(2-e^{-1})L_b}{2d}} . \tag{B21}$$

Finally, inserting equation (B21) into the imaginary part of equation (B20) and setting it equal to zero provides an equation for d/L_b as a function of μ_0. The best way to execute this final step is using a symbolic math program. The solution is

$$\frac{d}{L_b} = \frac{1}{8e}\left[\frac{(2e-1)(1-2e)^2}{\mu_0^2} - 1\right] + 1/4 \approx \left(\frac{2}{\mu_0}\right)^2 . \tag{B22}$$

Appendix C Dip-slip Faults

Consider an edge dislocation in a 2D homogeneous elastic body. The dislocation induces displacement and stress fields throughout the elastic body that can be represented in terms of two complex potentials, $\omega(z)$ and $\Omega(z)$, that are analytic functions of z (e.g. *England*, 2003; *Bower*, 2009). The complex coordinate z is defined as $z = x + iy = re^{i\phi}$ where (r, ϕ) are radial coordinates with ϕ measured from the x-axis in the direction of the y-axis.

For the dipping fault system shown in Figure 1C, the fault is located at $\beta_0 = \pi - \beta$ along $l \leq r \leq l + L$, where $l = d/\sin(\beta)$, (also note that $\xi = r$). The stress change functions can be obtained by considering a distribution of dislocations along the fault, and computing the shear and normal stresses that these dislocations induce on the fault itself. The first and most important step is to determine the complex potentials for a single dislocation placed at $z_0 = r_0 e^{i\beta_0}$, with Burger's vector $be^{i\beta_0} = b\cos(\beta_0) + ib\sin(\beta_0)$ (e.g. *Freund and Barnett*, 1976).

In the x-y plane the stress and displacement fields are given by:

$$\sigma_x + \sigma_y = 2\left[\Omega'(z) + \overline{\Omega'(z)}\right] , \tag{C1}$$

$$\sigma_y - i\sigma_{xy} = \Omega'(z) + \overline{\Omega'(z)} + z\overline{\Omega''(z)} + \omega'(z) , \tag{C2}$$

$$2G(u_x + iu_y) = (3 - 4\nu)\Omega(z) - z\overline{\Omega'(z)} - \overline{\omega(z)} , \tag{C3}$$

where primes denote derivatives with respect to z, and bars denote complex conjugates (e.g. Section 2.5 in *England*, 2003). The displacements are denoted by u_x, u_y; the normal stresses by σ_x and σ_y, and σ_{xy} is the shear stress. The normal and shear stresses on the fault can be obtained in the radial coordinate system, in which case the stresses are

$$\sigma_r + \sigma_\phi = 2\left[\Omega'(z) + \overline{\Omega'(z)}\right] , \tag{C4}$$

$$\sigma_\phi - i\sigma_{r\phi} = \Omega'(z) + \overline{\Omega'(z)} + e^{-2i\phi}[z\overline{\Omega''(z)} + \omega'(z)] , \tag{C5}$$

$$2G(u_r + iu_\phi) = e^{-2i\phi}[(3 - 4\nu)\Omega(z) - z\overline{\Omega'(z)} - \overline{\omega(z)}] . \tag{C6}$$

For a half-space with a traction-free surface at $y = 0$, $z = x$, the potentials can be written as

$$\Omega(z) = \Omega_0(z) + \Omega_1(z) , \qquad \omega(z) = \omega_0(z) + \omega_1(z) , \tag{C7}$$

where $\Omega_0(z)$ and $\omega_0(z)$ are the potentials for a full-space, and so will produce tractions along $z = x$; while $\Omega_1(z)$ and $\omega_1(z)$ are additional potentials that clear the tractions along $z = x$. The full-space potentials are given by (e.g. *Bower*, 2009, Section 5.3.12)

$$\Omega_0(z) = \gamma \ln (z - z_0) \, , \tag{C8}$$

$$\omega_0(z) = \overline{\gamma} \ln (z - z_0) - \frac{\gamma \overline{z}_0}{z - z_0} \, , \tag{C9}$$

where

$$\gamma = -\frac{iGbe^{i\beta_0}}{4\pi(1-\nu)} \, . \tag{C10}$$

The additional potentials can be found using a variety of methods (e.g. *Dmowska and Kostrov*, 1973; *Freund and Barnett*, 1976). Here, the additional potentials are computed using the process of analytic continuation (e.g. Section 3.5 in *England*, 2003), and are given by

$$\Omega_1(z) = -z\overline{\Omega_0'(\overline{z})} - \overline{\omega_0(\overline{z})} \, , \tag{C11}$$

$$\omega_1(z) = z\overline{\omega_0'(\overline{z})} - \overline{\Omega_0(\overline{z})} + z\overline{\Omega_0'(\overline{z})} + z^2\overline{\Omega_0''(\overline{z})} \, . \tag{C12}$$

Substituting these definitions for $\Omega_1(z)$ and $\omega_1(z)$ into equations (C7) along with the results for $\Omega_0(z)$ and $\omega_0(z)$, the potentials for an edge dislocation in a half-space are:

$$\Omega(z) = \gamma \ln \left[\frac{z - z_0}{z - \overline{z}_0} \right] - \frac{\overline{\gamma}(z - z_0)}{z - \overline{z}_0} \, , \tag{C13}$$

$$\omega(z) = \overline{\gamma} \ln \left[\frac{z - z_0}{z - \overline{z}_0} \right] - \frac{\gamma \overline{z}_0}{z - z_0} + \frac{\gamma z}{z - \overline{z}_0} + \frac{\overline{\gamma}(z_0 - \overline{z}_0) z}{(z - \overline{z}_0)^2} \, . \tag{C14}$$

Note that equations (A4) and (A5) in *Rudnicki and Wu* (1995) are the derivatives of equations (C13) and (C14).

The normal σ_ϕ and shear $\sigma_{r\phi}$ stresses on the fault due to a single dislocation are given by the real and imaginary parts of equation (C5), evaluated using equations (C13) and (C14) at values of z corresponding to $\phi = \beta_0$ and $l \leq \xi \leq l + L$. For a distribution of dislocations along the length of the fault, the resultant Burger's vector between neighboring points ξ and $\xi + d\xi$ is $b = (\partial\delta/\partial\xi)d\xi$, where $\delta(\xi)$ is slip on the fault (*Weertman*, 1996; *Freund and Barnett*, 1976). The stress change functions are found by integrating over the length of the fault, such that

$$T(\xi,\delta) = -\int_{l}^{l+L} \mathrm{Im}\left\{\Omega'(z) + \overline{\Omega'(z)} + e^{-2i\beta_0}[z\overline{\Omega''(z)} + \omega'(z)]\right\} \frac{\partial\delta}{\partial s} ds \;, \tag{C15}$$

$$N(\xi,\delta) = \int_{l}^{l+L} \mathrm{Re}\left\{\Omega'(z) + \overline{\Omega'(z)} + e^{-2i\beta_0}[z\overline{\Omega''(z)} + \omega'(z)]\right\} \frac{\partial\delta}{\partial s} ds \;, \tag{C16}$$

where the potentials are evaluated using equations (C13) and (C14) at $z = \xi e^{i\beta_0}$ and $z_0 = s e^{i\beta_0}$. Finally, note that it is possible to write the integrands in equations (C15) and (C16) explicitly in terms of ξ and β_0, however the resulting expressions are extremely cumbersome [see for example equations (13) in *Freund and Barnett* (1976); equations (3.1) – (3.2) in *Dmowska and Kostrov* (1973); or equations (A6) – (A11L) in *Rudnicki and Wu* (1995)]. For numerical computations it is most concise to compute the stresses using the individual equations listed above.